ISSN 0915-633X

NATIONAL INSTITUTE FOR FUSION SCIENCE

Three-Dimensional Simulation Study of the Magnetohydrodynamic Relaxation Process in the Solar Corona. II.

Y. Suzuki, K. Kusano and K. Nishikawa

(Received - Aug. 8, 1996)

NIFS-434 Aug. 1996

RESEARCH REPORT
NIFS Series

NAGOYA, JAPAN

THREE-DIMENSIONAL SIMULATION STUDY OF THE MAGNETOHYDRODYNAMIC RELAXATION PROCESS IN THE SOLAR CORONA. II.

Y. Suzuki
Theory and Computer Simulation Center, National Institute for Fusion Science,
Toki 509-52, Japan

and

K. Kusano and K. Nishikawa
Department of Materials Science, Faculty of Science, Hiroshima University,
Higashi-hiroshima 739, Japan

ABSTRACT

Three dimensional dynamics of solar coronal magnetic loops, which is caused by the photospheric twisting motion, is investigated in detail by using magnetohydrodynamic numerical simulations. It is found that as a result of the rising of the magnetic loops, isolated flux tubes (plasmoids) are generated on the top of the loops through magnetic reconnection. During the reconnection process, the magnetic energy of the mode coupled with the potential field is partially converted into the mode decoupled from it. We also analyze the linear stability of the coupled mode and reveal that it is destabilized when the loop height and the magnetic helicity exceed the critical values predicted from the bifurcation theory (Kusano et al. 1995). Furthermore, we reveal that three dimensional mode couplings have an effect to concentrate the helicity into an unstable mode, as well as an effect to reduce the growth rate of the instability.

Keywords: MHD — Sun: corona — Sun: flares — Sun: magnetic field

1. Introduction

The coronal magnetic field is believed to play crucial roles in various solar coronal phenomena (solar flare, prominence formation, coronal heating and so on). During about a last decade a lot of theorists have attempted to reveal the physical mechanism of these phenomena. Among them, the magnetohydrodynamic (MHD) energy relaxation model based on the Woltjer-Taylor minimum energy principle (Woltjer 1958; Taylor 1974) has been one of the most important theories to understand the physics of coronal plasmas (Heyvaerts & Priest 1984; Browning, Sakurai, & Priest 1986; Browning & Priest 1986; Browning 1988; Browning & Hood 1989; Démoulin et al. 1989; Démoulin & Priest 1989, 1992; Priest & Forbes 1990; Amari & Aly 1990, 1992; Démoulin, Raadu, & Malherbe 1992; Démoulin, Cuperman, & Semel 1992). The Woltjer-Taylor minimum energy principle is based on a hypothesis that, when the electric conductivity is finite but very high, the magnetic energy

$$E = \frac{1}{2\mu_0}\int_V \boldsymbol{B}\cdot\boldsymbol{B}dV, \tag{1}$$

must more quickly decay compared with the magnetic helicity

$$H = \int_V \boldsymbol{A}\cdot\boldsymbol{B}dV, \tag{2}$$

where the integration covers the whole volume V on interest, and $\boldsymbol{A}$ is the vector potential,

$$\nabla\times\boldsymbol{A} = \boldsymbol{B}. \tag{3}$$

Consequently, the minimum energy state is given by the linear force free field (LFFF):

$$\nabla\times\boldsymbol{B} = \alpha\boldsymbol{B}, \tag{4}$$

where α is a constant in space. In our previous paper (Kusano et al. 1994, hereafter paper 1), we reveal that, if the twisting motion at the photosphere injects the magnetic energy as well as the magnetic helicity into coronal magnetic loops, which are periodically aligned, the magnetic loops spontaneously organize a large-scale structure parallel to the magnetic inversion line. In paper 1, this process is regarded as a quasi-static evolution following a series of LFFFs, that is a continuous energy relaxation process consistent with the Woltjer-Taylor minimum energy principle.

Afterward, Kusano, Suzuki, & Nishikawa (1995; hereafter paper 2) found that, the Woltjer-Taylor minimum energy state in the coronal geometry bifurcates into two different solutions when the magnetic helicity H or the geometrical factor a (which is defined as the ratio of the height to the width of the domain) becomes larger than a certain value.

These solutions correspond to the coupled solution and the mixed solution described in Jensen & Chu (1984) and Taylor (1986), respectively. The coupled solution consists only of the components coupled with the potential field and the mixed solution is given by a mixture of the coupled solution and the components decoupled from the potential field. We theoretically proposed that solar flares could be understood as the transition from the former to the latter. Furthermore, Kusano, Suzuki, & Nishikawa (1995) predicted that the transition must be triggered by the upward stretch of the coronal magnetic loops.

In paper 1, although the spontaneous formation of the coupled state was observed, the transition into the mixed state was not seen. It might be due to the fact that the vertical length of the simulation box is too short for the magnetic loops to rise higher than the criterion for the bifurcation. In paper 2, using a larger simulation domain whose height is three times extended than that in paper 1, we could observe that the system leaves the branch of the coupled state and approaches the mixed state.

The objective in this paper is to investigate the three dimensional (3D) effects in that transition process. Particularly, we focus ourselves on two subjects: the 3D effects in the linear stability, and the 3D mode couplings in the nonlinar dynamics.

In the next section the simulation model will be briefly explained. Typical simulation results will be shown in § 3 about the magnetic field structure (§ 3.1), the helicity and energy dynamics (§ 3.2), and the nonlinear coupling among several Fourier modes (§ 3.3). The dependence on the electric resistivity as well as on the photospheric speed will be considered in § 3.4. In § 4, we will discuss the effects of the 3D nonlinear couplings in the energy relaxation process. Finally, a couple of important results will be summarized in § 5.

2. Simulation model

The simulation model is almost the same as in paper 1, except that the height of the simulation box is extended three times. The simulation box is given by a rectangular domain, inside of which corresponds to the coronal region (Fig.1(a)). Magnetic bipolar regions are periodically located on the photospheric boundary ($z = 0$), and in these regions we assume a twisting motion. For further details of the bottom boundary condition, see Eqs.(10) and (11) in paper 1. The upper boundary is assumed as a perfectly conducting wall and the periodic conditions are employed for the lateral boundaries. The ratio among each size of the box is given by $L_x : L_y : L_z = 1 : 1 : 6$.

The governing equations are given by

$$\rho\frac{\partial \boldsymbol{V}}{\partial t} = -\rho\nabla\cdot\boldsymbol{V}\boldsymbol{V} + \boldsymbol{J}\times\boldsymbol{B} - \nabla\cdot\Pi\,, \tag{5}$$

$$\frac{\partial \boldsymbol{B}}{\partial t} = -\nabla\times\boldsymbol{E}\,, \tag{6}$$

$$\boldsymbol{E} = -\boldsymbol{V}\times\boldsymbol{B} + \eta\boldsymbol{J}\,, \tag{7}$$

$$\boldsymbol{J} = \nabla\times\boldsymbol{B}\,, \tag{8}$$

$$\Pi = \nu[\frac{2}{3}(\nabla\cdot\boldsymbol{V})\boldsymbol{I} - \nabla\boldsymbol{V} - {}^t(\nabla\boldsymbol{V})]\,. \tag{9}$$

In these equations above, we adopt a zero β approximation in which the plasma density ρ and the pressure p are constant in space and time. This approximation is not so unreasonable for the coronal model, since the plasma β in coronae is usually much smaller than unity (for example, if $B = 100\mathrm{G}$, $n = 10^9\mathrm{cm}^{-3}$, and $T = 10^6\mathrm{K}$, then $\beta = 3\times10^{-4}$). The equations (5) through (9) have a nondimensional form, in which the density, the magnetic field, the velocity, the length, and the time are normalized by the coronal density ρ_0, the half value of the maximum strength in the photospheric magnetic field B_0, the characteristic Alfvén speed $V_A = (B_0^2/\mu_0\rho_0)^{\frac{1}{2}}$, the scale of the domain L_x, and the Alfvén transit time $\tau_A = L_x/V_A$, respectively. The viscosity ν is fixed to 1.0×10^{-3} in the normalized unit $(\rho_0 L_x V_A)$. We carry out several runs with various values of the resistivity η and the photospheric rotating period T_r. Table 1 summarizes the parameters for each run, in which case F2 will be reported in detail in the following section. Initially, the magnetic field is given by a potential field ($\nabla\times\boldsymbol{B} = 0$) and the plasma is at rest ($\boldsymbol{V} = 0$). The finite difference method with the second order accuracy and the Runge-Kutta-Gill method are used to solve the basic equations.

To examine the numerical resolution in space, we carried out the simulation F1′, in which the grid number for each dimension is 40 % enhanced compared with F1. The difference of the resultant magnetic energy between F1 and F1′ is up to about 7 %. Since case F1 has the sharpest current sheet on the reconnection point in all runs, the finite difference error in the other cases might be smaller than it.

3. Simulation results

3.1. Structure of magnetic field

Figures 2(a)-(p) display the evolution of iso-surfaces for the vector potential A_x in case F2. After the upward extension (Figs.2(a) and (b)), the arcade is subject to magnetic reconnection, which ejects a plasmoid upward (Figs.2(b) and (c)). The color on the plane

$x = 0$ reflects the length of the magnetic field lines across it. Particularly, the field lines across the red area are detached from the photosphere, hence this area implies the cross section of plasmoid. Figure 2(b) shows that the detached region already appears in the top of the arcade at $t = 50\tau_A$, and it is enlarged from $t = 50\tau_A$ to $60\tau_A$ (Fig.2(b) through (d)) as reconnection progresses.

We can observe that two reconnection sites exist, one being on the mid plane $y = L_y/2$ and the other being on the lateral plane $y = 0$ (or L_y). Reconnections take place alternately on these planes. From $t = 72\tau_A$ to $104\tau_A$ (Fig.2(f) through (i)), it proceeds on the lateral plane and a new plasmoid is generated. From $t = 106\tau_A$ to $134\tau_A$ (Fig.2(j) through (m)), the reconnection site is switched again onto the mid plane and it moves back to the lateral plane at $t = 136\tau_A$ (Fig.2(n)). As a result of these processes, the iso-surface for A_x forms a horizontal structure above the arcades.

Figure 3 shows the time evolution for the amount of the flux crossing the plane $x = 0$ which is detached from the bottom boundary $z = 0$, where the positive and the negative fluxes are separately plotted. In case F2, the positive flux comes up from $50\tau_A$ to $60\tau_A$, and then the negative flux begins to increase from $72\tau_A$ to $86\tau_A$. After that, the positive flux steps up from $106\tau_A$ to $116\tau_A$, and the negative flux increases again from $136\tau_A$. We can see that the increment of the positive and the negative flux corresponds to reconnections on the mid and the lateral plane, respectively.

These results clearly indicate that magnetic reconnection successively proceeds and generates isolated plasmoids dynamically. It is much consistent with the theoretical prediction that the plasmoid is generated on the top of the original loops as a result of the rising of the magnetic loops (see Fig.5 in paper 2).

3.2. Helicity and energy evolution

As shown in paper 2, the relevant parameters for the bifurcation of the minimum energy state are the helicity H and the geometrical factor a. Here, let us directly examine the evolution of them.

Figure 4 shows the trajectory on the parameter space consisting of the magnetic helicity and the height of the magnetic loops. The magnetic helicity is calculated from the equation (2) where the whole simulation box is taken as the integral domain V. The height of the magnetic loops is evaluated from the upward propagation of the photospheric information, which is carried by the MHD waves and also the plasma motion. In our simulation we observe that the magnetosonic shock wave is formed and it moves upward.

Thus, we recognize the altitude of the shock front as the loop height. The trajectory of case F2 reaches to the bifurcation curve at $t = 16\tau_A$, and enters into the region where the lowest energy state is given by the mixed solution. Here, it should be pointed out that there is some delay between the time for the bifurcation ($t = 16\tau_A$) and the time for the first reconnection ($t = 50 \sim 70\tau_A$) as discussed in Kusano, Suzuki et al. (1996).

Figure 5 shows the relationship between the energy and the helicity. Case F2 evolves following the branch of the coupled solution until $t = 50\tau_A$. This process is much similar to the results reported in paper 1. After that, however, while the helicity continues to increase, the increase of the energy is saturated. The trajectory enters into the lower energy region than the coupled solution.

3.3. Fourier mode evolution

Let us investigate the dynamics of the magnetic energy for each Fourier mode. The magnetic energy can be expanded as follows:

$$E = \sum_{m,n} \varepsilon_{m,n} = \sum_{m,n} \frac{1}{2}(L_x L_y) \int |\tilde{\boldsymbol{b}}_{m,n}(z)|^2 dz, \tag{10}$$

where $\tilde{\boldsymbol{b}}_{m,n}(z) = (L_x L_y)^{-1} \int_0^{Ly} \int_0^{Lx} \boldsymbol{B} \exp[2\pi i(mx/L_x + ny/L_y)] dxdy$ with integers m and n. Figure 6 shows the time history of $\varepsilon_{m,n}$ for most dominant three modes: $(m,n) = (0,0), (0,1)$ and $(1,0)$, in those only the $(0,1)$ mode is coupled with the potential field, and the $(0,0)$ and the $(1,0)$ modes are decoupled from it. We can see that the amplitude of the $(0,0)$ mode grows up comparable to the $(0,1)$ mode by $t = 140\tau_A$. On the other hand, the evolution of the $(1,0)$ mode is oscillatory and the amplitude is at most about 1% of the $(0,0)$ mode. This result implies that the final state is the mixed state which consists mainly of the $(0,1)$ and the $(0,0)$ modes.

In order to study in detail the growth of the $(0,0)$ mode, we calculate the rate at which the magnetic energy is transferred from each mode into the $(0,0)$ mode. The evolution of $\varepsilon_{0,0}$ can be described as

$$\dot{\varepsilon}_{0,0} \equiv \frac{d\varepsilon_{0,0}}{dt} = \dot{\varepsilon}^C_{0,0} + \dot{\varepsilon}^I_{0,0} + \dot{\varepsilon}^D_{0,0} \ , \tag{11}$$

where $\dot{\varepsilon}^C_{0,0}$, $\dot{\varepsilon}^I_{0,0}$, and $\dot{\varepsilon}^D_{0,0}$ imply the contributions from the mode coupling, from the energy injection at the boundary, and from the diffusion, respectively:

$$\dot{\varepsilon}^C_{0,0} = \sum_{m,n} \dot{\varepsilon}^C_{m,n\to 0,0} = \sum_{m,n} Re \int \tilde{\boldsymbol{v}}_{m,n} \times \tilde{\boldsymbol{b}}_{-m,-n} \cdot \tilde{\boldsymbol{j}}_{0,0} dV \ , \tag{12}$$

$$\dot{\varepsilon}^I_{0,0} = \sum_{m,n} \dot{\varepsilon}^I_{m,n\to 0,0} = \sum_{m,n} Re \int (\tilde{\boldsymbol{b}}_{0,0} \cdot \tilde{\boldsymbol{v}}_{m,n}) \tilde{\boldsymbol{b}}_{-m,-n} \cdot d\boldsymbol{S} \ , \tag{13}$$

$$\dot{\varepsilon}^D_{0,0} = -Re \int \eta |\tilde{\boldsymbol{j}}_{0,0}|^2 dV \ . \tag{14}$$

Figure 7 shows the history of $\dot{\varepsilon}^C_{m,n-0,0}$ for $(m,n) = (0,0)$, $(0,1)$, and $(1,0)$, in which the positive (negative) value means that the energy of the (m,n) mode flows into (out of) the $(0,0)$ mode. The largest contribution in the mode couplings comes from the $(0,1)$ mode. The negative contribution of the $(0,0)$ mode stands for the process that the magnetic energy of the $(0,0)$ mode flows into the kinetic energy of the same mode. Furthermore, the smallness of the $(1,0)$ mode indicates that the $(0,0)$ mode hardly couples with the $(1,0)$ mode. The diffusion always gives a negative contribution to the growth of the $(0,0)$ mode. These results suggest that the $(0,1)$ mode must be unstable against the $(0,0)$ mode perturbation.

Here, we calculate the linear growth rate of the $(0,1)$ mode γ^* based on the mode selecting procedure (Kusano & Nishikawa 1996a), and show the result in Fig.8, where the error bar represents the convergence error in an iterative procedure. We can see that after $t = 14\tau_A$ the growth rate is positive. Note that this time almost coincides with the time when the trajectory in Fig.4 crosses the bifurcation curve. It implies that the $(0,1)$ mode is immediately destabilized when the arcade configuration satisfies the bifurcation condition.

This is in agreement with the conclusion of Kusano & Nishikawa (1996a), who reveal that the coupled solution is unstable if the mixed solution for the same helicity can exist. Actually, the instability observed here is the symmetric mode instability (SMI) found in Kusano & Nishikawa (1996a), and it may be the same instability as observed in two dimensional simulations (Mikic et al. 1988; Biskamp & Welter 1989, Kusano, Suzuki et al. 1996). On the other hand, we did not observe the so-called undulating mode instability (UMI) (Kusano & Nishikawa 1996a), although the undulating modes $m \neq 0$ are included in our model. It might be due to the fact that the length of the simulation box L_x is shorter than the criterion for the UMI. The UMI must be marginally stable in our model.

3.4. Parameter dependence

In the most other runs, we can observe the results similar to observed in F2: the generation of the detached flux through the reconnection process (see Fig.3), the satisfaction of the bifurcation condition for the helicity and the loop height (see Fig.4), and the appearance of the lower energy state than the coupled solution branch (see Fig.5). Only

in case F3, however, magnetic reconnection does not take place, so that the detached flux remains almost zero. In that case, the trajectory in Fig.5(b) stays above the branch of the coupled solution. The speciality of F3 might be due to the large resistivity.

If we compare the results among the simulations which have the same resistivity (between F1 and S1 or between F2 and S2), we can see that both the magnetic helicity and the loop height are more quickly enlarged for shorter T_r. As a result of it, the larger magnetic energy is stored until the onset of reconnection. On the other hand, when the photospheric speed is fixed, the larger energy could be accumulated in more conductive case. It is due to the fact that the decay of the total helicity is slower for the smaller resistivity.

Note that the helicity evolution is governed by the following equation,

$$\frac{dH}{dt} = \int (\boldsymbol{E} \times \boldsymbol{A} - \phi \boldsymbol{B}) \cdot d\boldsymbol{S} - \int \eta \boldsymbol{J} \cdot \boldsymbol{B} dV \ , \tag{15}$$

where the first term is given by the surface integral on the photospheric boundary. Although the helicity injection denoted by the first term of the right-hand side does not depend on the resistivity, the resistive dissipation (the second term) is obviously proportional to the resistivity. Then, the remaining helicity and the energy must depend on the resistivity as discussed in the previous paragraph. However, when the magnetic Reynolds number is so large as in the real corona, it is likely that the second term of (15) becomes negligibly small. In that case, the dependence of the instability on the resistivity must be more important (Kusano, Suzuki et al. 1996). Since the growth rate of the instability decreases with resistivity (Kusano & Nishikawa 1996b), even if the helicity dissipation is negligibly small, the tendency that the larger energy can be accumulated before the reconnection process as the resistivity decreases may survive.

4. Discussion

4.1. Stability

Kusano & Nishikawa (1996a) show that the coupled solution is unstable against $n = 0$ modes if the bifurcation condition is satisfied. In some case (F3), however, we cannot observe the reconnection process though it satisfies the bifurcation condition. This fact suggests that the instability in the 3D system might be more complicated than the result of Kusano & Nishikawa (1996a), in which particular modes are extracted for the analysis.

Now, we analyze the stability in the 3D system using three different methods: The first method is the calculation of the nonlinear growth rate Γ for the $(m, n) = (0, 0)$ mode,

which is obtained directly from the nonlinear simulation data, $\Gamma = d \ln \varepsilon_{0,0}/dt$. The second method is the calculation of the most unstable linear growth rate γ in the 3D system. It is obtained by solving the 3D eigenvalue problem,

$$\gamma \begin{pmatrix} \rho_0 \boldsymbol{V}_1 \\ \boldsymbol{B}_1 \end{pmatrix} = \begin{pmatrix} \boldsymbol{J}_0 \times \boldsymbol{B}_1 + \boldsymbol{J}_1 \times \boldsymbol{B}_0 - \nabla \cdot \Pi_1 \\ \nabla \times (\boldsymbol{V}_1 \times \boldsymbol{B}_0 - \eta \boldsymbol{J}_1) \end{pmatrix} , \tag{16}$$

$$\boldsymbol{J}_0 = \nabla \times \boldsymbol{B}_0 , \qquad \boldsymbol{J}_1 = \nabla \times \boldsymbol{B}_1 , \tag{17}$$

$$\Pi_1 = \nu [\frac{2}{3} (\nabla \cdot \boldsymbol{V}_1) \boldsymbol{I} - \nabla \boldsymbol{V}_1 - {}^t (\nabla \boldsymbol{V}_1)] , \tag{18}$$

where $\boldsymbol{B}_0$ is the magnetic field given by the simulation result. Equations (16) to (18) are numerically solved with the conventional power method. The third method is the calculation of the linear growth rate γ^* for the $(0,0)$ mode in terms of the mode extracting method used in Kusano & Nishikawa (1996a). The result is presented in Fig.8, where the history of Γ and γ^*, as well as the value of γ at $t = 50\tau_A$, are plotted. Initially the nonlinear growth rate Γ has a large value because the very small amplitude of the $(0,0)$ mode can be driven by the photospheric motion. After that, Γ quickly decreases and becomes smaller than γ^*, which comes up after $t = 14\tau_A$. The nonlinear growth rate is smaller than one half of γ^*. On the other hand, the 3D linear growth rate γ has a value close to Γ. It implies that, although the coupling between the $(0,1)$ and $(0,0)$ modes is still important for the instability even in the 3D system, other mode couplings included in the 3D system have a partially stabilizing effect.

4.2. Comparison with 2D system

To clearly understand the characteristics of the 3D system, let us compare the current simulation results with two dimensional (2D) dynamics. We carried out the 2D simulation, in which a translational symmetry $\partial/\partial x = 0$ is imposed (see Fig.1(b)) as in Mikic et al. (1988) and Biskamp & Welter (1989). The initial magnetic field is given by the $m = 0$ modes those are extracted from the initial field of the 3D simulation. The photospheric velocity pattern is also given by the $m = 0$ mode components extracted from the photospheric pattern in the 3D simulation, where the speed is adjusted so that the helicity injection rate into the $(m,n) = (0,1)$ mode is equivalent to that in the 3D simulation. Other all parameters are comparable to case F2.

The magnetic helicity can be represented in terms of the Fourier modes:

$$H = \sum_{m,n} h_{m,n} = \sum_{m,n} (L_x L_y) \int \tilde{\boldsymbol{a}}_{m,n}(z) \cdot \tilde{\boldsymbol{b}}_{-m,-n}(z) dz . \tag{19}$$

Similarly to the energy equation (11), the helicity evolution for the $(m,n) = (0,1)$ mode is affected by the mode coupling, by the injection from the boundary, and also by the diffusion, respectively:

$$\dot{h}_{0,1} \equiv \frac{dh_{0,1}}{dt} = \dot{h}^C_{0,1} + \dot{h}^I_{0,1} + \dot{h}^D_{0,1} \ , \tag{20}$$

where

$$\dot{h}^C_{0,1} = \sum_{m,n} \dot{h}^C_{m,n\to 0,1} = \sum_{m,n} Re \int 2(\tilde{\boldsymbol{v}}_{m,n} \times \tilde{\boldsymbol{b}}_{-m,1-n}) \cdot \tilde{\boldsymbol{b}}_{0,-1} dV \ , \tag{21}$$

$$\dot{h}^I_{0,1} = \sum_{m,n} \dot{h}^I_{m,n\to 0,1} = -\sum_{m,n} \int \{(\tilde{\boldsymbol{a}}_{0,-1} \cdot \tilde{\boldsymbol{v}}_{m,n})\tilde{\boldsymbol{b}}_{-m,1-n} - \tilde{\phi}_{0,-1}\tilde{\boldsymbol{b}}_{0,1}\} \cdot d\boldsymbol{S} \ , \tag{22}$$

and

$$\dot{h}^D_{0,1} = -Re \int 2\eta \tilde{\boldsymbol{j}}_{0,-1} \cdot \tilde{\boldsymbol{b}}_{0,1} dV \ . \tag{23}$$

Figure 9 shows the evolution of $\dot{h}^C_{0,1}$ and $\dot{h}^I_{0,1}$ in the 3D and 2D simulations. Notice that, although the same helicity is injected into the both simulations, the 3D simulation can generate much larger helicity for $(m,n) = (0,1)$ by the mode coupling effect than the 2D case. Therefore, we conclude that through the 3D mode couplings the helicity is concentrated into the arcade component $(m,n) = (0,1)$. Here, to detect the modes responsible to this process, we separately plot the effects of the $m \neq 0$ modes ($\sum_{m\neq 0} \dot{h}^C_{m,n\to 0,1}$) and the $m = 0$ modes ($\sum_{m=0} \dot{h}^C_{m,n\to 0,1}$) in Fig.9. We can see that the $m \neq 0$ modes always give a positive contribution. It means that the mode coupling with the $m \neq 0$ modes acts to generate the $(0,1)$ mode helicity. Figure 10(a) shows the integration of the helicity which has been injected into each mode until $t = 14\tau_A$, $\int_0^{14\tau_A} \dot{h}^I_{m,n} dt$. On the other hand, Fig.10(b) is the helicity spectrum of the minimum energy state, which has the same helicity as the simulation result at $t = 14\tau_A$. Those diagrams show that the spectrum of the injected helicity has a broader profile for m modes compared with the minimum energy state. Therefore, we can understand that the helicity concentration to the $(0,1)$ mode is necessary for the magnetic field to approach to the minimum enrgy state. This fact is consistent with our previous result that, through an MHD relaxation to the minimum energy state, a large scale magnetic field parallel to the magnetic inversion line is generated spontaneously (paper 1). It must be an inverse cascade process from $m \neq 0$ to $m = 0$ mode.

Not only for the helicity but also for the energy, the concentration into the $(0,1)$ mode is observed. Figure 11 shows the evolution of $\dot{\varepsilon}^C_{0,1}$ and $\dot{\varepsilon}^I_{0,1}$, where

$$\dot{\varepsilon}^C_{0,1} = \sum_{m,n} \dot{\varepsilon}^C_{m,n\to 0,1} = \sum_{m,n} Re \int \tilde{\boldsymbol{v}}_{m,n} \times \tilde{\boldsymbol{b}}_{-m,1-n} \cdot \tilde{\boldsymbol{j}}_{0,-1} dV \ , \tag{24}$$

$$\dot{\varepsilon}^I_{0,1} = \sum_{m,n} \dot{\varepsilon}^I_{m,n-0,1} = \sum_{m,n} Re \int (\tilde{\boldsymbol{b}}_{0,-1} \cdot \tilde{\boldsymbol{v}}_{m,n}) \tilde{\boldsymbol{b}}_{-m,1-n} \cdot d\boldsymbol{S} \ . \tag{25}$$

Although the injection from the boundary is not so largely different between the 3D and 2D simulations, the mode coupling in the 3D simulation is much larger than the 2D result. Likely for the helicity evolution, the contribution from the $m \neq 0$ modes ($\sum_{m\neq 0} \dot{\varepsilon}^C_{m,n\to 0,1}$) predominates. From these analyses, we can understand that, in the 3D system, an inverse cascade takes place, in which the high m mode components are transfered into the $(0,1)$ mode. Since this process enhances the helicity as well as the energy for the $(0,1)$ mode, it stimulates the instability. Furthermore, if the $(0,1)$ mode becomes unstable, the instability converts a part of the $(0,1)$ mode energy into the $(0,0)$ mode through the reconnection process shown in the previous section.

5. Summary

We investigated the 3D dynamics of the solar coronal magnetic loops by using MHD simulations. We can see that if the magnetic energy and the magnetic helicity are injected by the photospheric motion into the coronal magnetic loops, which are periodically aligned on the photosphere, the magnetic loops are expanded upward and the plasmoid is generated on the top of the original loops. Recently, the soft X-ray telescope (SXT) on board *Yohkoh* observes various solar phenomena, which strongly suggest magnetic reconnection (Hudson 1994). For instance, the plasmoid ejection is observed in some flare events (Ohyama et al. 1996). The simulation results are consistent with those observations.

The simulation results are consistent also with the theoretical prediction that the plasmoid should be generated as a result of the transition between the coupled solution and the mixed solution of the Woltjer-Taylor minimum energy state (Kusano et al. 1995). However, when the loop height exceeds the bifurcation criteria, the magnetic configuration does not immediately transit to the mixed solution but follows the coupled solution for a while. In this period the instability grows and the magnetic energy is accumulated in the coronal magnetic field. Furthermore, we revealed that the 3D couplings work to partially stabilize the instability. We also found that the 3D mode couplings play a role to concentrate the helicity as well as the energy into the arcade component through an inverse cascade process.

We thank Prof. T.Sato, Dr. H.Takamaru, Dr. A.Kageyama, Dr. T.H.Watanabe, from National Institute for Fusion Science for useful discussions. This research is supported by a Grant-in-Aid from the Ministry of Education, Science, and Culture in Japan.

Table 1. Parameters adopted in six simulation runs: The resistivity η, the period of the photospheric rotation T_r and the number of grid elements (n_x, n_y, n_z).

case	F1	F1′	F2	F3	S1	S2
η	0.5×10^{-3}	0.5×10^{-3}	1.0×10^{-3}	2.0×10^{-3}	0.5×10^{-3}	1.0×10^{-3}
T_r/τ_A	15	15	15	15	30	30
(n_x, n_y, n_z)	$(56, 56, 336)$	$(80, 80, 480)$	$(56, 56, 336)$	$(56, 56, 336)$	$(56, 56, 336)$	$(28, 28, 168)$

REFERENCES

Amari,T., & Aly,J.J. 1990, A&A, 231, 213

Amari,T., & Aly,J.J. 1992, A&A, 265, 791

Biskamp,D., & Welter,H. 1989, Sol. Phys., 120, 49

Browning,P.K., & Hood,A.W. 1989, Sol. Phys., 124, 271

Browning,P.K., & Priest,E.R. 1986, A&A, 159, 129

Browning,P.K., Sakurai,T., & Priest,E.R. 1986, A&A, 158, 217

Démoulin,P., Cuperman,S., & Semel,M. 1992, A&A, 263, 351

Démoulin,P., & Priest,E.R. 1989, A&A, 214, 360

Démoulin,P., & Priest,E.R. 1992, A&A, 258, 535

Démoulin,P., Priest,E.R., & Anzer,U. 1989, A&A, 221, 326

Démoulin,P., Raadu,M.A., & Malherbe,J.M. 1992, A&A, 257, 278

Heyvaerts,J., & Priest,E.R. 1984, A&A, 137, 63

Hudson,H. 1994, in Proc. of Kofu Symposium New Look at the Sun with Emphasis on Advanced Observations of Coronal Dynamics and Flares, ed. S.Enome & T.Hirayama NRO Report No. 360, 1

Jensen,T., & Chu,M.S. 1984, Phys. Fluids, 27, 2881

Kusano,K., Suzuki,Y., Kubo,H., Miyoshi,T., & Nishikawa,K. 1994, ApJ, 433, 361

Kusano,K., Suzuki,Y., & Nishikawa,K. 1995, ApJ, 441, 942

Kusano,K., Suzuki, Y., Fujie, K., Endo, Y., & Nishikawa, K. 1996, 'Solar Flare as Taylor's Relaxation', to be published in PASP

Kusano,K., & Nishikawa,K. 1996a, ApJ, 461, 415

Kusano,K., & Nishikawa,K. 1996b, 'Simulation Study of Magnetic Reconnection in Solar Corona', to be published in PASP

Mikic,Z., Barnes,D.C., & Schnack,D.D. 1988, ApJ, 328, 830

Ohyama,M., & Shibata,K. 1996, to be published in Proc. the IAU Colloquium No.153, Magnetodynamic Phenomena in the Solar Atmosphere, ed. Y.Uchida T.Kosugi & S.Hudson (Kluwer Academic Publishers)

Priest,E.R. & Forbes,T.G. 1990, Sol. Phys., 130, 399

Taylor,J.B. 1974, Phys. Rev. Lett., 33, 1139

Taylor,J.B. 1986, Rev. Mod. Phys., 58, 741

Woltjer,L. 1958, Proc. Nat. Acad. Sci. USA, 44, 489

This preprint was prepared with the AAS LaTeX macros v4.0.

Fig. 1.— The schematic diagram of the simulation box, in which the bottom boundary (plane $z = 0$) corresponds to the photosphere. (a) The simulation box in the 3D model and the magnetic loops in it. The magnetic bipolar region lies on the bottom, and it is twisted clockwise. (b) The simulation region in the 2D model, in which the translational symmetry is assumed for the x direction. The shearing motion is imposed on the bottom.

Fig. 2.— The black curve surface represents iso-value surfaces for the vector potential A_x in the three dimensional space, and the red area on the plane $x = 0$ implies where the field lines are detached from the photosphere. The color on the bottom plane reflects the strength of the magnetic field B_z there, showing the positive (blue) and negative (red) polarity regions. It can be seen that the flux tube (plasmoid) is formed on the top of the original loops. Here, notice that the iso-contours of A_x is not exactly same as the structure of the magnetic field lines in 3D cases.

Fig. 3.— The time evolution for the amount of the flux crossing the plane $x = 0$ which is detached from the plane $z = 0$.

Fig. 4.— The relationship between the magnetic helicity and the height of the magnetic loops. The small solid circles show the simulation results and the solid line is the bifurcation curve which is theoretically derived. The time when the bifurcation condition is satisfied is indicated.

Fig. 5.— The time evolution of the magnetic energy as well as the magnetic helicity. The small solid circles show the simulation results, where the time when the reconnection starts is indicated. The curve E_c and the line E_m represent the energy for the coupled and the mixed solutions, respectively. The small square region bounded by the dotted line in (a) is magnified in (b).

Fig. 6.— The time evolution of the magnetic energy for the $(0,0), (0,1)$ and $(1,0)$ modes, $\varepsilon_{0,0}$, $\varepsilon_{0,1}$, $\varepsilon_{1,0}$. The dashed line represents the total energy E.

Fig. 7.— The time history of the magnetic energy transport rate from three modes, $(m,n) = (0,1), (1,0), (0,0)$, into the $(0,0)$ mode ($\dot{\varepsilon}^C_{0,1\to 0,0}$, $\dot{\varepsilon}^C_{1,0\to 0,0}$, $\dot{\varepsilon}^C_{0,0\to 0,0}$) as well as the energy diffusion rate $\dot{\varepsilon}^D_{0,0}$ are plotted. The dashed line represents $\dot{\varepsilon}_{0,0}$.

Fig. 8.— The time history of the growth rate. The dashed line represents the linear growth rate γ^* calculated by the mode selecting method. The solid line represents the nonlinear growth rate Γ for $\varepsilon_{0,0}$. The open circle represents the linear growth rate γ calculated in the three dimensional system.

Fig. 9.— The changing rates of the magnetic helicity for the $(0,1)$ mode are plotted both for

the 3D and 2D simulations, where the mode coupling ($\dot{h}^{C\,3D}_{0,1}$ and $\dot{h}^{C\,2D}_{0,1}$) and the injection from the boundary ($\dot{h}^{I\,3D}_{0,1}$ and $\dot{h}^{I\,2D}_{0,1}$) are separately plotted.

Fig. 10.— (a) The power spectrum of the injected helicity until $t = 14\tau_A$ and (b) that of the minimum energy state which has the same helicity as the simulation at $t = 14\tau_A$ are displayed for $(-5, -5) \leq (m, n) \leq (5, 5)$.

Fig. 11.— The time history of the magnetic energy transport rate into the $(0, 1)$ mode is plotted both for the 3D and 2D simulations.

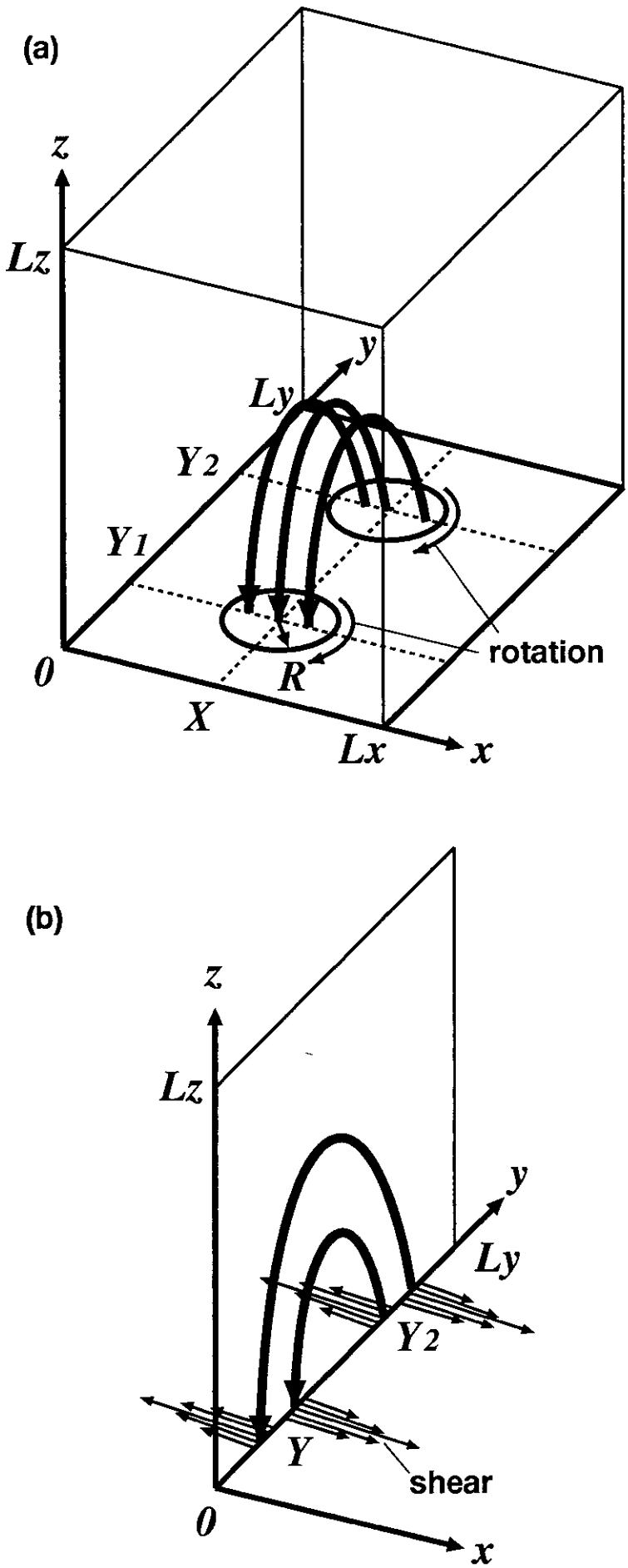

Figure 1:

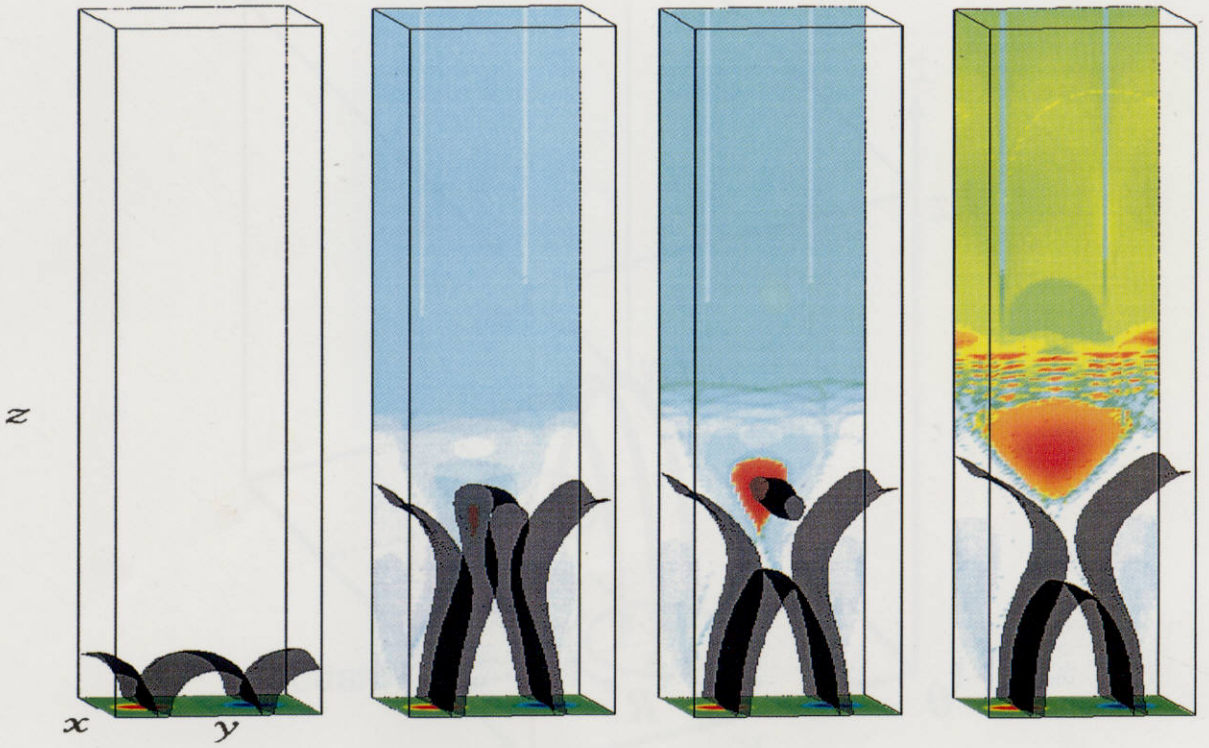
z
x
y
(a) t=0 τA
(b) t=50τA
(c) t=54τA
(d) t=60τA

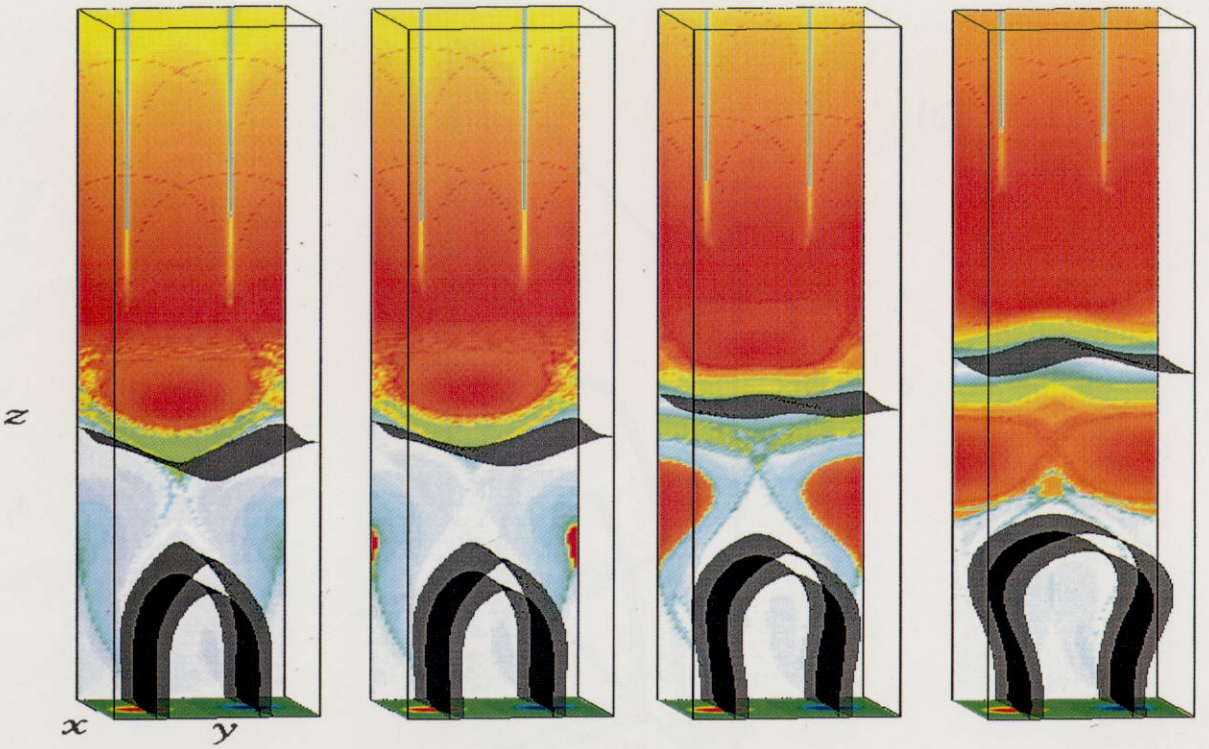
z
x
y
(e) t=70τA
(f) t=72τA
(g) t=80τA
(h) t=90τA

Figure 2:

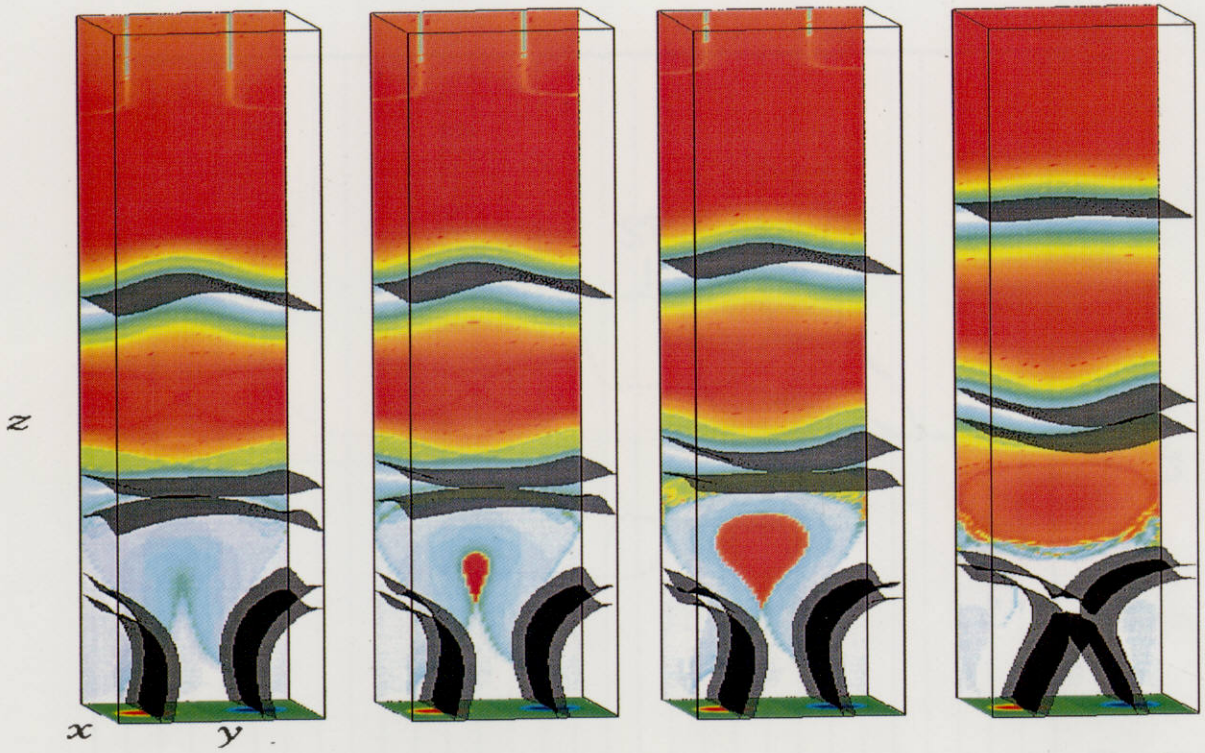
z
x
y
(i) t=104τA (j) t=106τA (k) t=110τA (l) t=120τA


z
x
y
(m) t=134τA (n) t=136τA (o) t=138τA (p) t=140τA

Figure 2:

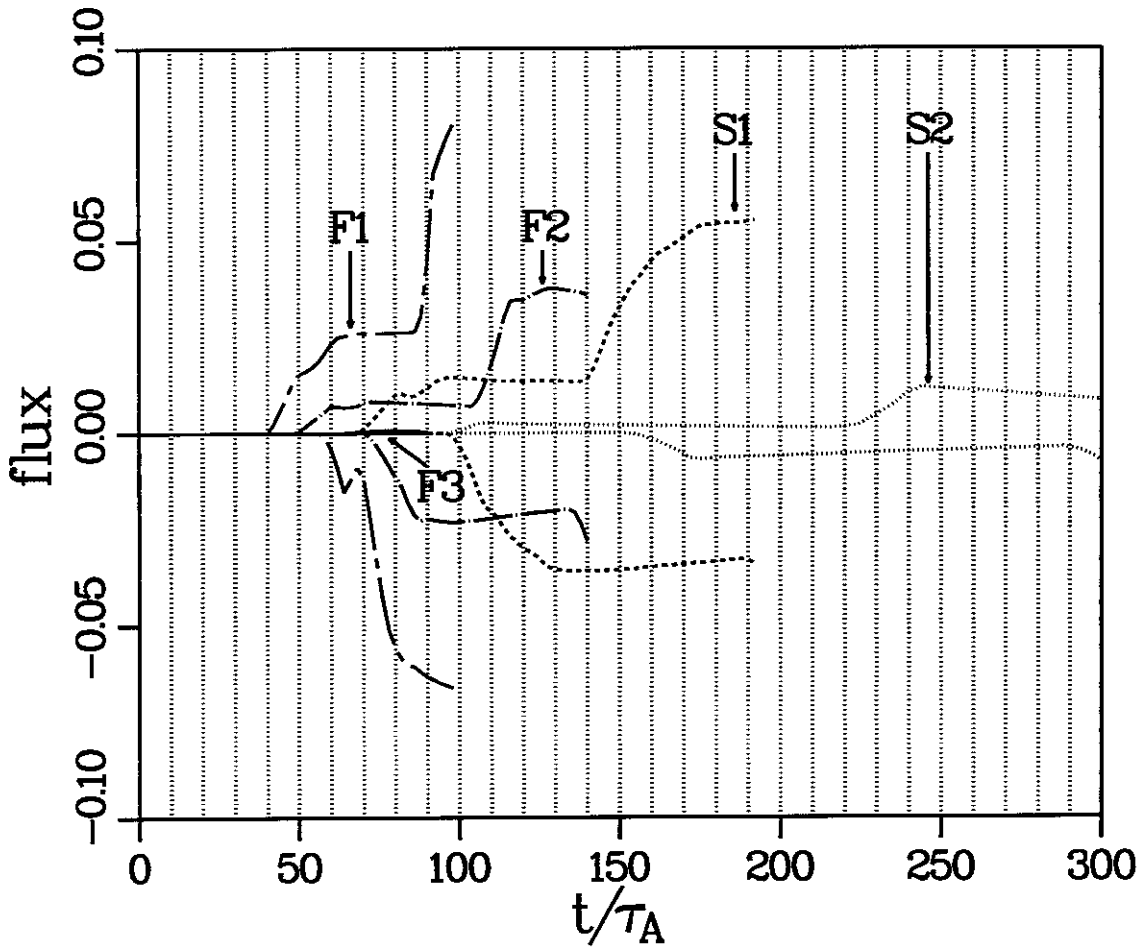
flux
0.10
0.05
0.00
−0.05
−0.10
0
50
100
150
200
250
300
t/τ_A
F1
F2
F3
S1
S2

Figure 3:

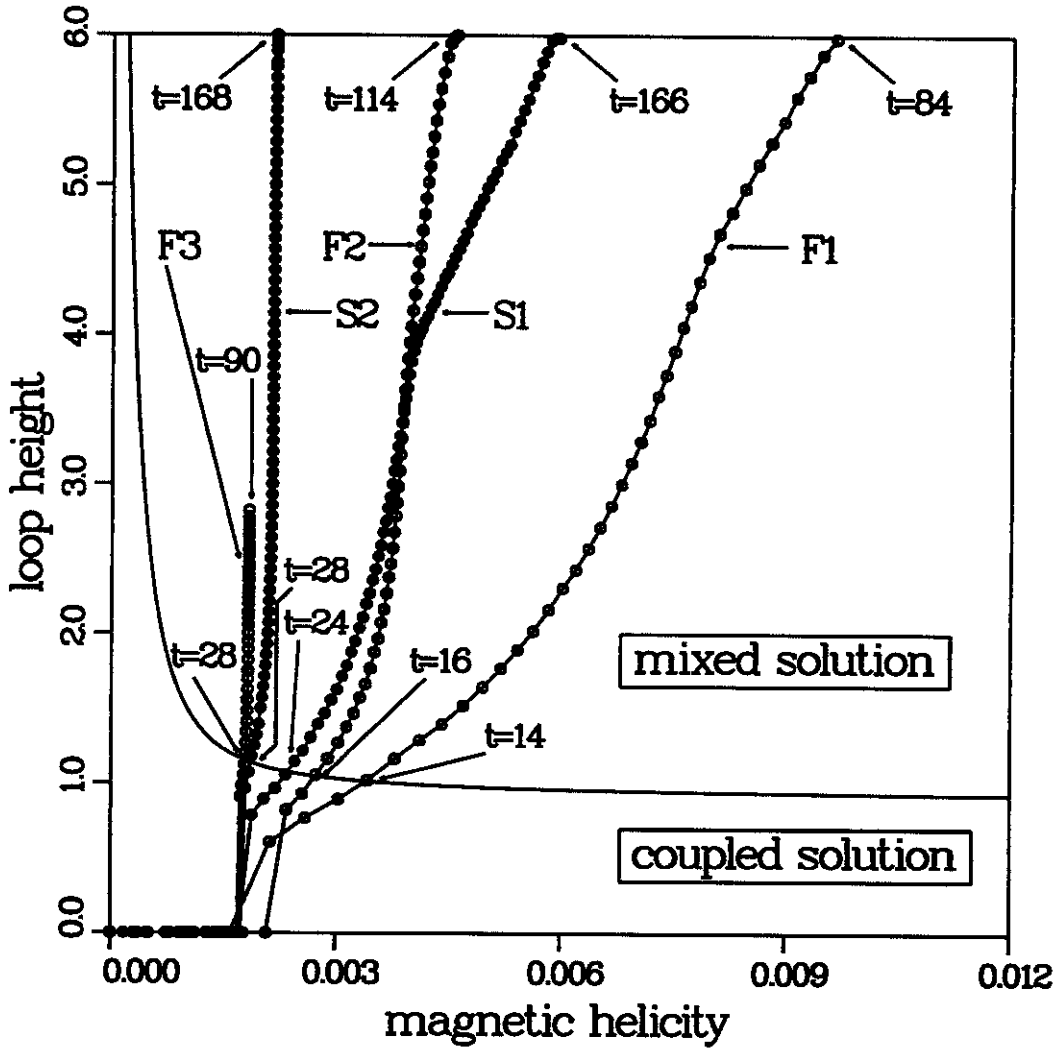
t=168
t=114
t=166
t=84
F3
F2
F1
S2
S1
t=90
t=28
t=24
t=28
t=16
t=14
mixed solution
coupled solution
loop height
magnetic helicity
0.0
1.0
2.0
3.0
4.0
5.0
6.0
0.000
0.003
0.006
0.009
0.012

Figure 4:

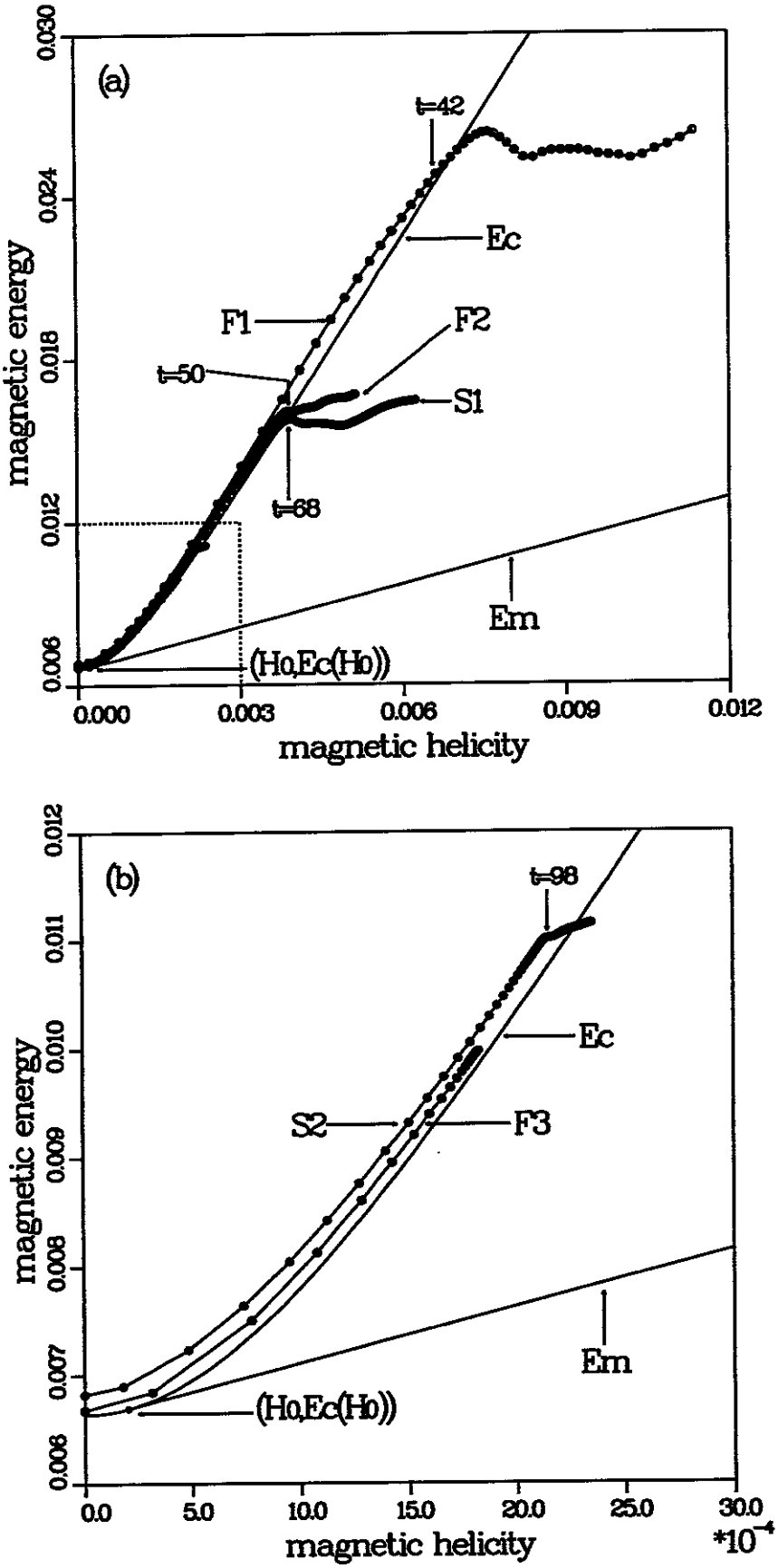
(a)
t=42
Ec
F1
F2
t=50
S1
t=68
Em
(H0,Ec(H0))
magnetic energy
magnetic helicity
0.030
0.024
0.018
0.012
0.006
0.000
0.003
0.006
0.009
0.012
(b)
t=98
Ec
S2
F3
Em
(H0,Ec(H0))
magnetic energy
magnetic helicity
0.012
0.011
0.010
0.009
0.008
0.007
0.006
0.0
5.0
10.0
15.0
20.0
25.0
30.0
*10^-4

Figure 5:

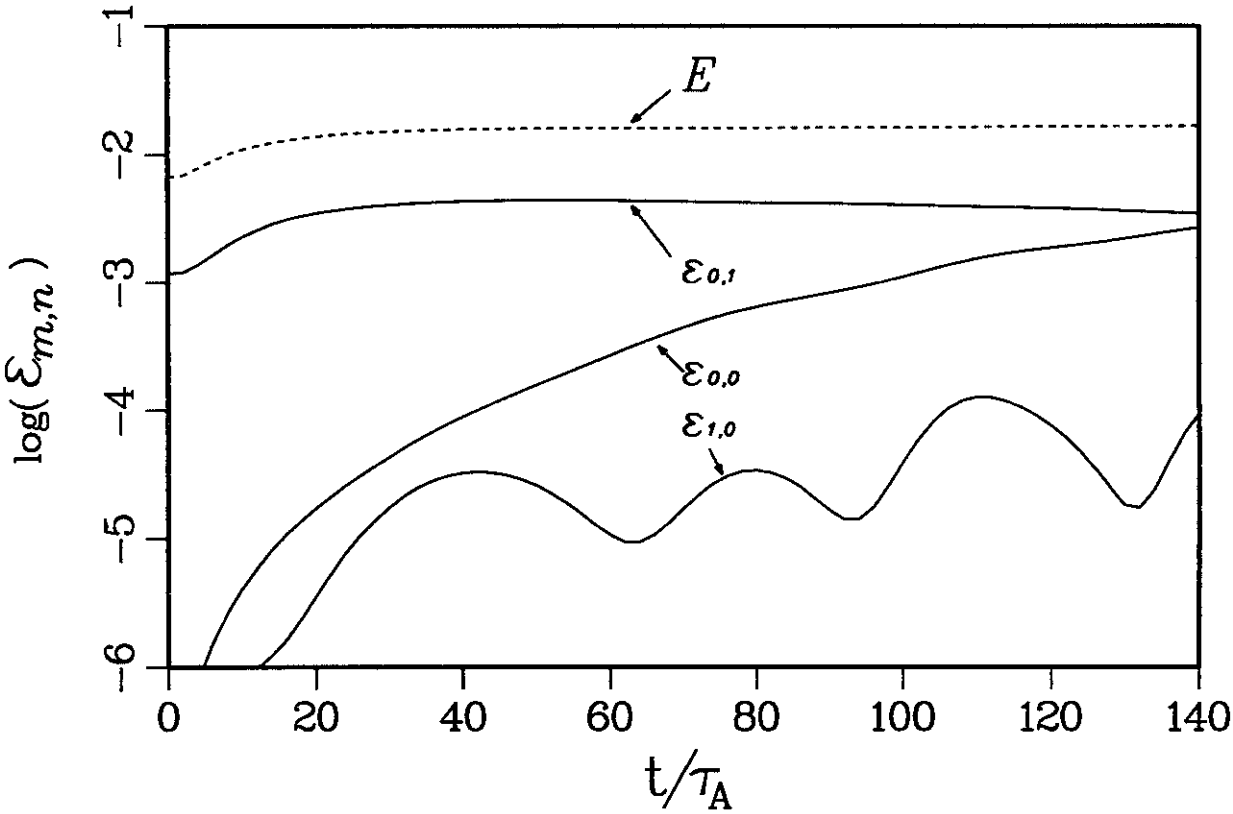
E
$\mathcal{E}_{0,1}$
$\mathcal{E}_{0,0}$
$\mathcal{E}_{1,0}$
log($\mathcal{E}_{m,n}$)
-1
-2
-3
-4
-5
-6
0
20
40
60
80
100
120
140
t/τ_A

Figure 6:

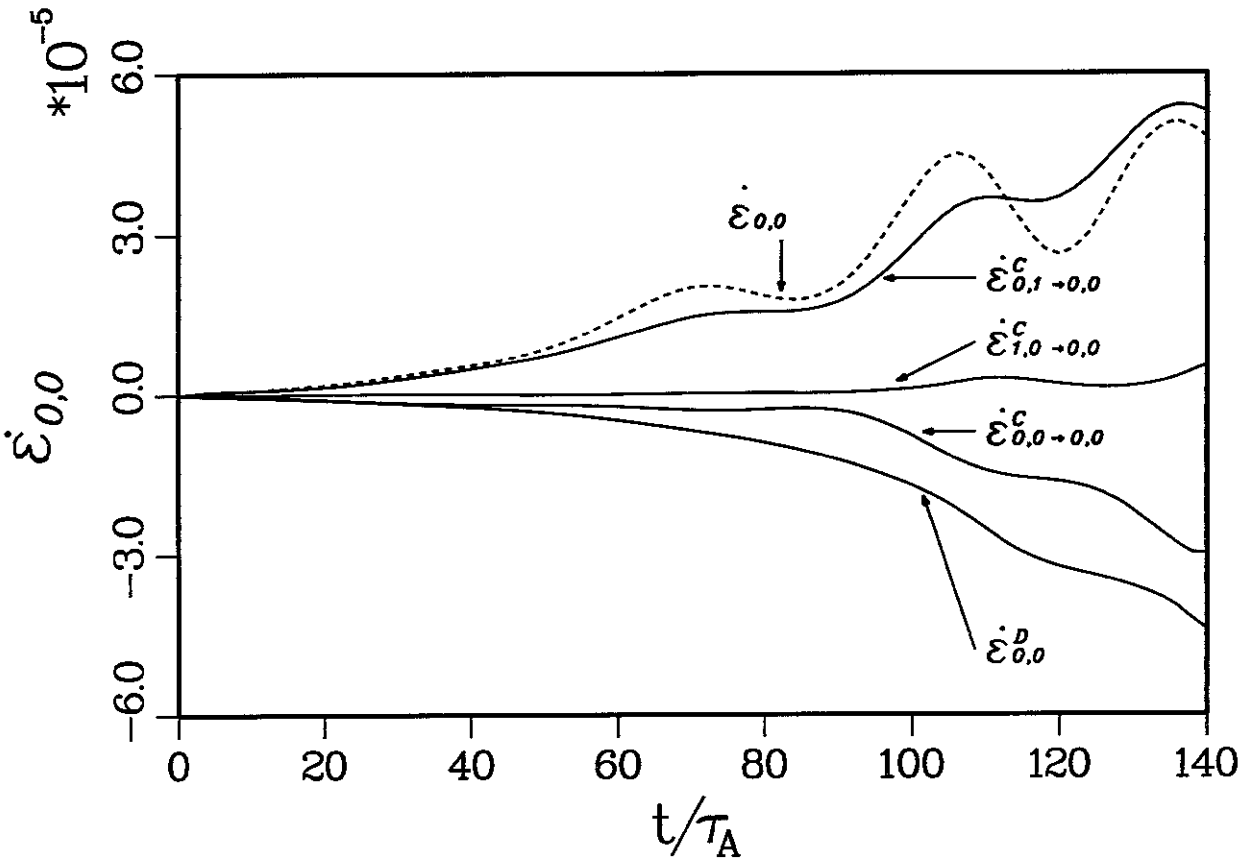
*10^-5
6.0
3.0
0.0
-3.0
-6.0
$\dot{\varepsilon}_{0,0}$
0
20
40
60
80
100
120
140
t/τ_A
$\dot{\varepsilon}_{0,0}$
$\dot{\varepsilon}^{C}_{0,1\to 0,0}$
$\dot{\varepsilon}^{C}_{1,0\to 0,0}$
$\dot{\varepsilon}^{C}_{0,0\to 0,0}$
$\dot{\varepsilon}^{D}_{0,0}$

Figure 7:

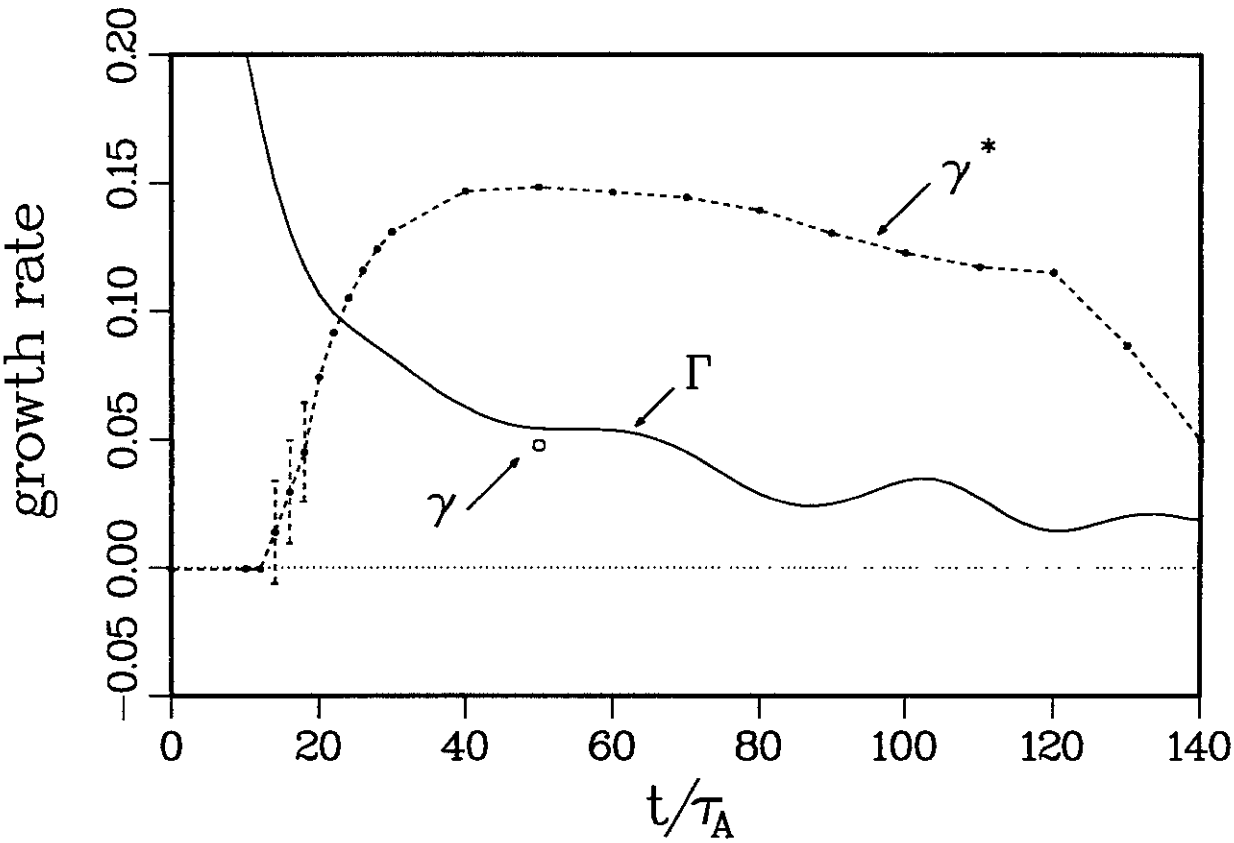
growth rate
0.20
0.15
0.10
0.05
0.00
−0.05
0
20
40
60
80
100
120
140
t/τA
γ*
Γ
γ

Figure 8:

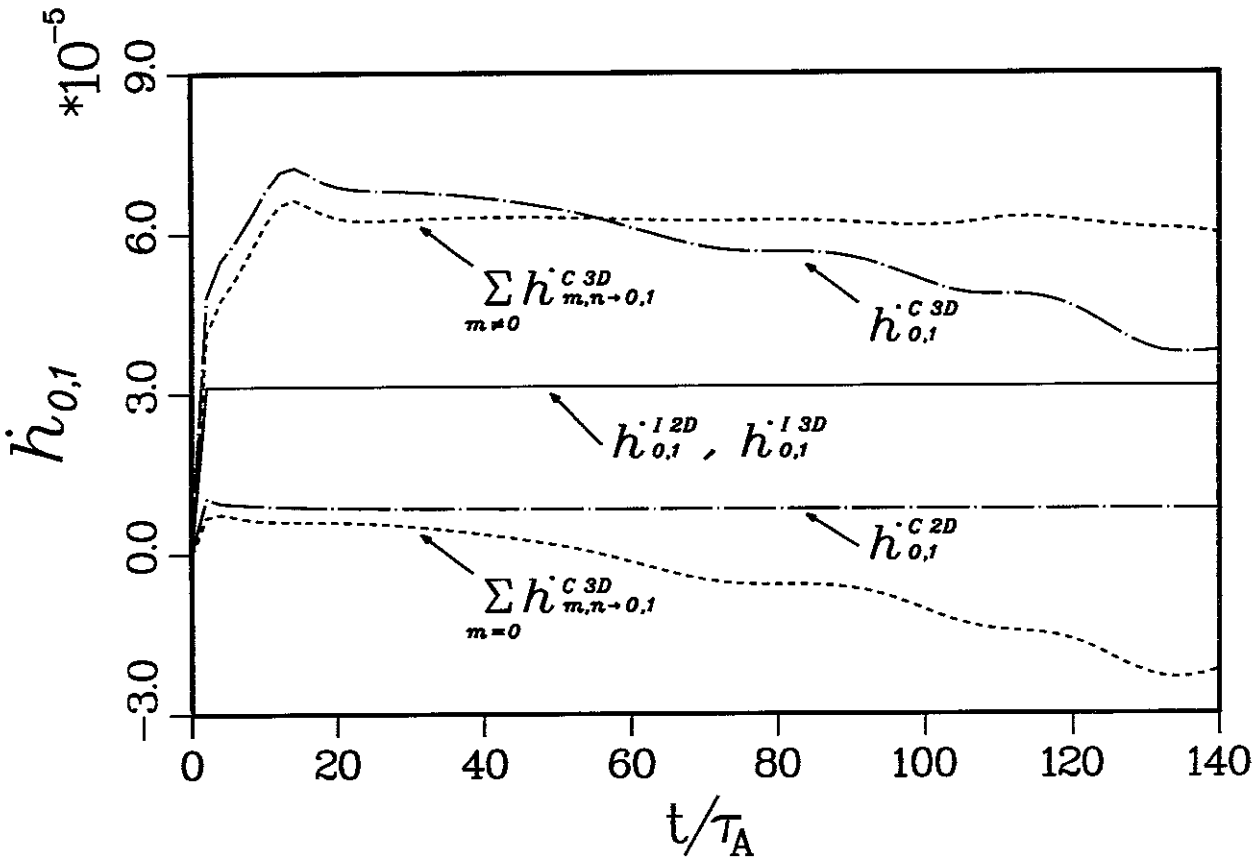
*10^-5
9.0
6.0
3.0
0.0
-3.0
ḣ0,1
Σ ḣ C 3D m,n→0,1 (m≠0)
ḣ C 3D 0,1
ḣ I 2D 0,1 , ḣ I 3D 0,1
ḣ C 2D 0,1
Σ ḣ C 3D m,n→0,1 (m=0)
0
20
40
60
80
100
120
140
t/τA

Figure 9:

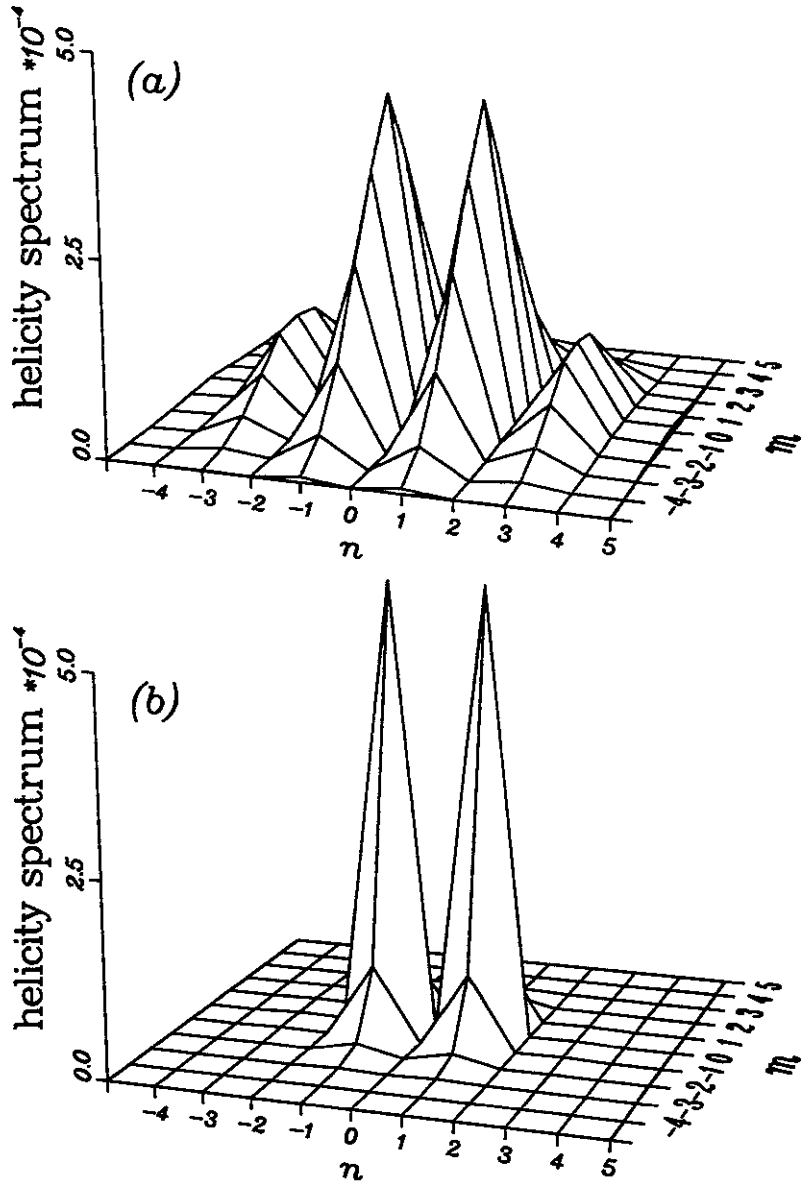

Figure 10:

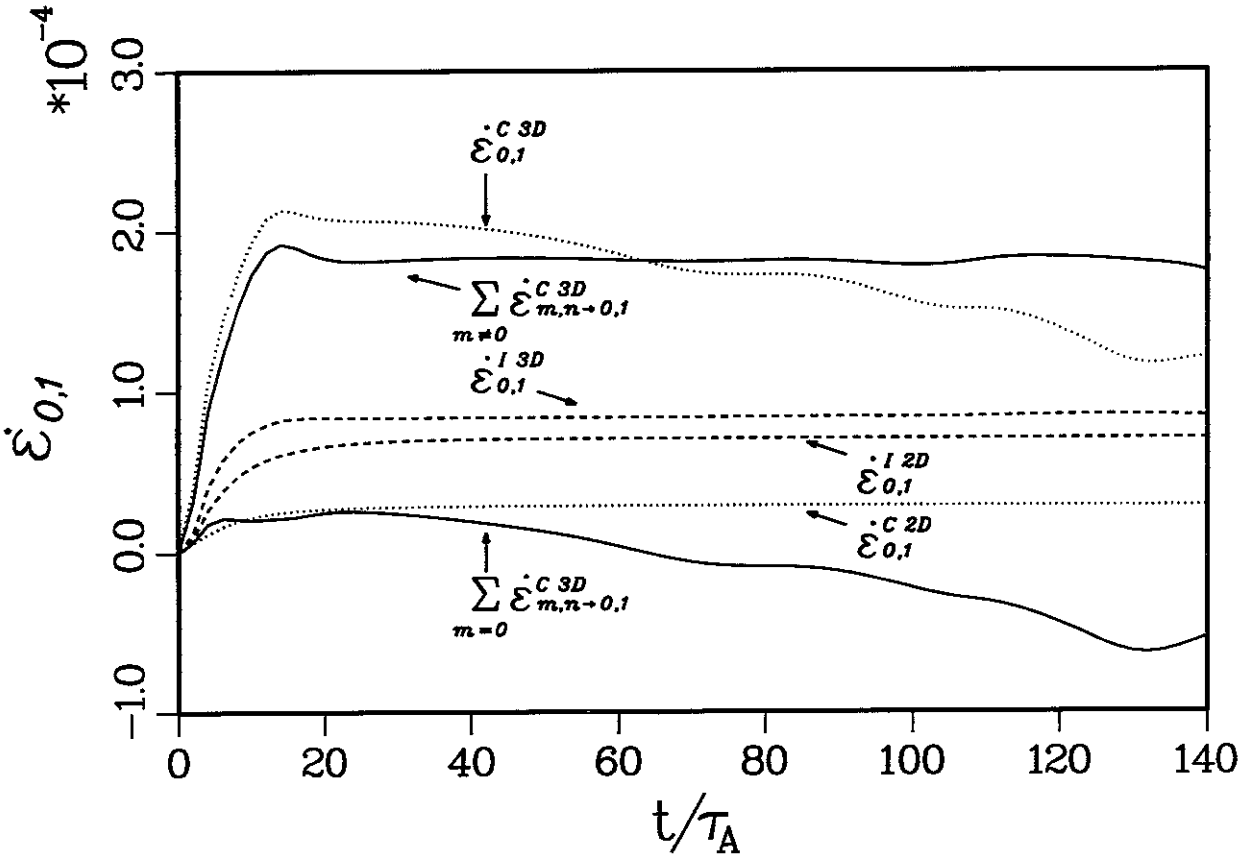
*10^-4
3.0
2.0
1.0
0.0
-1.0
0
20
40
60
80
100
120
140
t/τ_A
ε̇ 0,1
ε̇ C 3D 0,1
Σ ε̇ C 3D m,n→0,1 m≠0
ε̇ I 3D 0,1
ε̇ I 2D 0,1
ε̇ C 2D 0,1
Σ ε̇ C 3D m,n→0,1 m=0

Figure 11:

Recent Issues of NIFS Series

NIFS-389 K. Akaishi,
On the Outgassing Rate Versus Time Characteristics in the Pump-down of an Unbaked Vacuum System; Dec. 1995

NIFS-390 K.N. Sato, S. Murakami, N. Nakajima, K. Itoh,
Possibility of Simulation Experiments for Fast Particle Physics in Large Helical Device (LHD); Dec. 1995

NIFS-391 W.X.Wang, M. Okamoto, N. Nakajima, S. Murakami and N. Ohyabu,
A Monte Carlo Simulation Model for the Steady-State Plasma in the Scrape-off Layer; Dec. 1995

NIFS-392 Shao-ping Zhu, R. Horiuchi, T. Sato and The Complexity Simulation Group,
Self-organization Process of a Magnetohydrodynamic Plasma in the Presence of Thermal Conduction; Dec. 1995

NIFS-393 M. Ozaki, T. Sato, R. Horiuchi and the Complexity Simulation Group
Electromagnetic Instability and Anomalous Resistivity in a Magnetic Neutral Sheet; Dec. 1995

NIFS-394 K. Itoh, S.-I Itoh, M. Yagi and A. Fukuyama,
Subcritical Excitation of Plasma Turbulence; Jan. 1996

NIFS-395 H. Sugama and M. Okamoto, W. Horton and M. Wakatani,
Transport Processes and Entropy Production in Toroidal Plasmas with Gyrokinetic Eletromagnetic Turbulence; Jan. 1996

NIFS-396 T. Kato, T. Fujiwara and Y. Hanaoka,
X-ray Spectral Analysis of Yohkoh BCS Data on Sep. 6 1992 Flares - Blue Shift Component and Ion Abundances -; Feb. 1996

NIFS-397 H. Kuramoto, N. Hiraki, S. Moriyama, K. Toi, K. Sato, K. Narihara, A. Ejiri, T. Seki and JIPP T-IIU Group,
Measurement of the Poloidal Magnetic Field Profile with High Time Resolution Zeeman Polarimeter in the JIPP T-IIU Tokamak; Feb. 1996

NIFS-398 J.F. Wang, T. Amano, Y. Ogawa, N. Inoue,
Simulation of Burning Plasma Dynamics in ITER; Feb. 1996

NIFS-399 K. Itoh, S-I. Itoh, A. Fukuyama and M. Yagi,
Theory of Self-Sustained Turbulence in Confined Plasmas; Feb. 1996

NIFS-400 J. Uramoto,
A Detection Method of Negative Pionlike Particles from a H2 Gas Descharge Plasma; Feb. 1996

NIFS-401 K.Ida, J.Xu, K.N.Sato, H.Sakakita and JIPP TII-U group,
Fast Charge Exchange Spectroscopy Using a Fabry-Perot Spectrometer in the JIPP TII-U Tokamak; Feb. 1996

NIFS-402 T. Amano,
Passive Shut-Down of ITER Plasma by Be Evaporation; Feb. 1996

NIFS-403 K. Orito,
A New Variable Transformation Technique for the Nonlinear Drift Vortex; Feb. 1996

NIFS-404 T. Oike, K. Kitachi, S. Ohdachi, K. Toi, S. Sakakibara, S. Morita, T. Morisaki, H. Suzuki, S. Okamura, K. Matsuoka and CHS group; *Measurement of Magnetic Field Fluctuations near Plasma Edge with Movable Magnetic Probe Array in the CHS Heliotron/Torsatron*; Mar. 1996

NIFS-405 S.K. Guharay, K. Tsumori, M. Hamabe, Y. Takeiri, O. Kaneko, T. Kuroda,
Simple Emittance Measurement of H- Beams from a Large Plasma Source; Mar. 1996

NIFS-406 M. Tanaka and D. Biskamp,
Symmetry-Breaking due to Parallel Electron Motion and Resultant Scaling in Collisionless Magnetic Reconnection; Mar. 1996

NIFS-407 K. Kitachi, T. Oike, S. Ohdachi, K. Toi, R. Akiyama, A. Ejiri, Y. Hamada, H.Kuramoto, K. Narihara, T. Seki and JIPP T-IIU Group,
Measurement of Magnetic Field Fluctuations within Last Closed Flux Surface with Movable Magnetic Probe Array in the JIPP T-IIU Tokamak; Mar. 1996

NIFS-408 K. Hirose, S. Saito and Yoshi.H. Ichikawa
Structure of Period-2 Step-1 Accelerator Island in Area Preserving Maps; Mar. 1996

NIFS-409 G.Y.Yu, M. Okamoto, H. Sanuki, T. Amano,
Effect of Plasma Inertia on Vertical Displacement Instability in Tokamaks; Mar. 1996

NIFS-410 T. Yamagishi,
Solution of Initial Value Problem of Gyro-Kinetic Equation; Mar. 1996

NIFS-411 K. Ida and N. Nakajima,
Comparison of Parallel Viscosity with Neoclassical Theory; Apr. 1996

NIFS-412 T. Ohkawa and H. Ohkawa,
Cuspher, A Combined Confinement System; Apr. 1996

NIFS-413 Y. Nomura, Y.H. Ichikawa and A.T. Filippov,
Stochasticity in the Josephson Map; Apr. 1996

NIFS-414 J. Uramoto,
Production Mechanism of Negative Pionlike Particles in H_2 Gas Discharge Plasma; Apr. 1996

NIFS-415 A. Fujisawa, H. Iguchi, S. Lee, T.P. Crowley, Y. Hamada, S. Hidekuma, M. Kojima,
Active Trajectory Control for a Heavy Ion Beam Probe on the Compact Helical System; May 1996

NIFS-416 M. Iwase, K. Ohkubo, S. Kubo and H. Idei
Band Rejection Filter for Measurement of Electron Cyclotron Emission during Electron Cyclotron Heating; May 1996

NIFS-417 T. Yabe, H. Daido,T. Aoki, E. Matsunaga and K. Arisawa,
Anomalous Crater Formation in Pulsed-Laser-Illuminated Aluminum Slab and Debris Distribution; May 1996

NIFS-418 J. Uramoto,
Extraction of K^- Mesonlike Particles from a D_2 Gas Discharge Plasma in Magnetic Field; May 1996

NIFS-419 J. Xu, K. Toi, H. Kuramoto, A. Nishizawa, J. Fujita, A. Ejiri, K. Narihara, T. Seki, H. Sakakita, K. Kawahata, K. Ida, K. Adachi, R. Akiyama, Y. Hamada, S. Hirokura, Y. Kawasumi, M. Kojima, I. Nomura, S. Ohdachi, K.N. Sato
Measurement of Internal Magnetic Field with Motional Stark Polarimetry in Current Ramp-Up Experiments of JIPP T-IIU; June 1996

NIFS-420 Y.N. Nejoh,
Arbitrary Amplitude Ion-acoustic Waves in a Relativistic Electron-beam Plasma System; July 1996

NIFS-421 K. Kondo, K. Ida, C. Christou, V.Yu.Sergeev, K.V.Khlopenkov, S.Sudo, F. Sano, H. Zushi, T. Mizuuchi, S. Besshou, H. Okada, K. Nagasaki, K. Sakamoto, Y. Kurimoto, H. Funaba, T. Hamada, T. Kinoshita, S. Kado, Y. Kanda, T. Okamoto, M. Wakatani and T. Obiki,
Behavior of Pellet Injected Li Ions into Heliotron E Plasmas; July 1996

NIFS-422 Y. Kondoh, M. Yamaguchi and K. Yokozuka,
Simulations of Toroidal Current Drive without External Magnetic Helicity Injection; July 1996

NIFS-423 Joong-San Koog,
Development of an Imaging VUV Monochromator in Normal Incidence Region: July 1996

NIFS-424 K. Orito,
A New Technique Based on the Transformation of Variables for Nonlinear

Drift and Rossby Vortices; July 1996

NIFS-425 A. Fujisawa, H. Iguchi, S. Lee, T.P. Crowley, Y. Hamada, H. Sanuki, K. Itoh, S. Kubo, H. Idei, T. Minami, K. Tanaka, K. Ida, S. Nishimura, S. Hidekuma, M. Kojima, C. Takahashi, S. Okamura and K. Matsuoka,
Direct Observation of Potential Profiles with a 200keV Heavy Ion Beam Probe and Evaluation of Loss Cone Structure in Toroidal Helical Plasmas on the Compact Helical System; July 1996

NIFS-426 H. Kitauchi, K. Araki and S. Kida,
Flow Structure of Thermal Convection in a Rotating Spherical Shell; July 1996

NIFS-427 S. Kida and S. Goto,
Lagrangian Direct-interaction Approximation for Homogeneous Isotropic Turbulence; July 1996

NIFS-428 V.Yu. Sergeev, K.V. Khlopenkov, B.V. Kuteev, S. Sudo, K. Kondo, F. Sano, H. Zushi, H. Okada, S. Besshou, T. Mizuuchi, K. Nagasaki, Y. Kurimoto and T. Obiki,
Recent Experiments on Li Pellet Injection into Heliotron E; Aug. 1996

NIFS-429 N. Noda, V. Philipps and R. Neu,
A Review of Recent Experiments on W and High Z Materials as Plasma-Facing Components in Magnetic Fusion Devices; Aug. 1996

NIFS-430 R.L. Tobler, A. Nishimura and J. Yamamoto,
Design-Relevant Mechanical Properties of 316-Type Stainless Steels for Superconducting Magnets; Aug. 1996

NIFS-431 K. Tsuzuki, M. Natsir, N. Inoue, A. Sagara, N. Noda, O. Motojima, T. Mochizuki, T. Hino and T. Yamashina,
Hydrogen Absorption Behavior into Boron Films by Glow Discharges in Hydrogen and Helium; Aug. 1996

NIFS-432 T.-H. Watanabe, T. Sato and T. Hayashi,
Magnetohydrodynamic Simulation on Co- and Counter-helicity Merging of Spheromaks and Driven Magnetic Reconnection; Aug. 1996

NIFS-433 R. Horiuchi and T. Sato,
Particle Simulation Study of Collisionless Driven Reconnection in a Sheared Magnetic Field; Aug. 1996

NIFS-434 Y. Suzuki, K. Kusano and K. Nishikawa,
Three-Dimensional Simulation Study of the Magnetohydrodynamic Relaxation Process in the Solar Corona. II.; Aug. 1996